

This figure "f2.jpg" is available in "jpg" format from:

<http://arxiv.org/ps/astro-ph/9907233v1>

This figure "f3a.jpg" is available in "jpg" format from:

<http://arxiv.org/ps/astro-ph/9907233v1>

This figure "f3b.jpg" is available in "jpg" format from:

<http://arxiv.org/ps/astro-ph/9907233v1>

This figure "f4.jpg" is available in "jpg" format from:

<http://arxiv.org/ps/astro-ph/9907233v1>

This figure "f5a.jpg" is available in "jpg" format from:

<http://arxiv.org/ps/astro-ph/9907233v1>

This figure "f5b.jpg" is available in "jpg" format from:

<http://arxiv.org/ps/astro-ph/9907233v1>

Signatures of the Youngest Starbursts: Optically-thick Thermal Bremsstrahlung Radio Sources in Henize 2-10

Henry A. Kobulnicky¹
 University of California, Santa Cruz
 Santa Cruz CA, 95064
 Electronic Mail: chip@ucolick.org

Kelsey E. Johnson
 JILA
 University of Colorado
 Boulder CO 80309-0440
 Electronic Mail: kjohnson@casa.colorado.edu
Accepted for Publication in the Astrophysical Journal

ABSTRACT

VLA radio continuum imaging reveals compact (<8 pc) ~ 1 mJy radio sources in the central $5''$ starburst region of the blue compact galaxy Henize 2-10. While the global radio continuum spectrum is a power law ($S_\nu \propto \nu^\alpha$) indicative of nonthermal processes ($\alpha \simeq -0.5$), the radio sources have positive ($\alpha > 0.0$) spectral indices suggesting an optically thick thermal bremsstrahlung origin. We model the luminosities and spectral energy distributions of these radio knots, finding that they are consistent with unusually dense H II regions having electron densities, $1500 \text{ cm}^{-3} < n_e < 5000 \text{ cm}^{-3}$, and sizes $3 \text{ pc} < R < 8 \text{ pc}$. While the high inferred densities are typical of ultracompact H II regions in the Galaxy, such high optical depth ($\tau = 0.4 - 3.0$ at 5 GHz) at frequencies as high as 5 GHz is unusual on pc scales in galaxies. Since these H II regions are not visible in optical images, we propose that the radio data preferentially reveal the youngest, densest, and most highly obscured starforming events. Energy considerations imply that each of the five H II regions contains ~ 750 O7V equivalent stars, greater than the number found in 30 Doradus in the LMC. The high densities imply an over-pressure compared to the typical interstellar medium so that such objects must be short-lived (< 0.5 Myr expansion timescales). We conclude that the radio continuum maps reveal

¹Hubble Fellow

the very young (< 0.5 Myr) precursors of “super starclusters” or “proto globular clusters” which are prominent at optical and UV wavelengths in He 2-10 and elsewhere. The fraction of O stars in these ultra-dense H II regions is 15% of the total inferred O star population in He 2-10. This body of work leads us to propose that massive extragalactic star clusters with ages $< 10^6$ yr, the possible precursors to globular clusters, may be most easily identified by finding compact radio sources with optically-thick thermal bremsstrahlung spectral signatures.

Subject headings: Galaxies: individual: Henize 2-10 — galaxies: ISM — galaxies: star clusters — galaxies: starburst — HII Regions — stars: Wolf-Rayet

1. Introduction

The blue compact galaxy Henize 2-10 has been extensively studied as the prototype of starbursting galaxies containing large populations of Wolf-Rayet stars (e.g., Conti 1991). Morphological studies reveal at least three distinct starforming regions, termed A, B, and C as show recently in the images of Méndez *et al.* (1999). Each region is composed of numerous < 10 pc sized OB star clusters (Conti & Vacca 1994; Johnson *et al.* 1999). Optical and 21-cm radial velocities of $v_{\odot} = 860\text{-}870$ km s $^{-1}$ (RC3; Allen, Wright, & Goss 1976) suggest a distance between 6 Mpc (Johansson 1987) and 14 Mpc (Allen *et al.* 1976) depending on the choice of H_0 and Virgocentric inflow models. Thus, the apparent B-band magnitudes of 12.4 (RC3) to 11.8 (Johansson *et al.* 1987) result in absolute magnitudes ranging from $M_B = -16.5$ (dwarf) to $M_B = -18.9$ ($\sim 0.6 L_*$).² Assuming the oft-adopted distance³ of 9 Mpc, the optical diameter of 60" (RC3) corresponds to 2.8 kpc, making He 2-10 a comparatively compact galaxy. The HI rotation curve is solid body in nature, and single-peaked, with a velocity dispersion ($\sigma_v \equiv FWHM/2.35$) of 68 km s $^{-1}$ (Allen *et al.* 1976; Kobulnicky *et al.* 1995). These properties make He 2-10 similar to some of the compact star-forming galaxies seen at intermediate redshifts (Koo *et al.* 1995; Guzman *et al.* 1996, 1998) and in the Hubble Deep Field (Phillips *et al.* 1997).

He 2-10 contains several $\times 10^8 M_{\odot}$ of molecular gas (Baas, Israel & Koornneef 1994; Kobulnicky *et al.* 1995; Meier & Turner 1999) and shows evidence for large amounts of dust

² For $M_{*B} = -19.4$ as found by Marzke *et al.* 1998.

³The current distance uncertainty propagates into large uncertainties on other physical parameters including the star formation rate and young star population. Further work on He 2-10 would be greatly aided by a new distance determination based on methods other than the radial velocity.

obscuration (Philips *et al.* 1984; Beck, Kelly, & Lacy 1997). This high dust and molecular content is consistent with the strong CO emission and with recent chemical abundance measurements indicating a metallicity of nearly the solar value (Kobulnicky, Kennicutt, & Pizagno 1995). $H\alpha$ images of Henize 2-10 show multiple ionized shells and filaments (Beck & Kovo 1999; Méndez *et al.* 1999) typical of actively starforming systems which may be undergoing starburst-driven outflows (e.g. Marlowe *et al.* 1995; Martin 1998). Single-dish radio continuum measurements over a range of frequencies show a dominant nonthermal component, suggesting the presence significant supernova activity (Allen *et al.* 1976).

In this paper we present a spatially-resolved radio continuum study of He 2-10 using multi-configuration data from the Very Large Array (VLA)⁴. We consider the overall radio continuum energy distribution in light of other recent work on this galaxy, and we analyze high-resolution (0.5'') radio maps of the central starburst in conjunction with HST imaging of Johnson *et al.* (1999).

2. VLA Radio Continuum Observations

Aperture synthesis radio continuum observations were carried out with the NRAO Very Large Array using a variety of frequencies and array configurations from 1984 December through 1996 January. Table 1 summarizes dates, configurations, frequencies, and durations of observations. The first four datasets in Table 1 are part of a program to measure the total radio flux at coarse (6'') resolution using “scaled-arrays” which provide similar UV coverage at 92 cm, 21 cm, 6 cm, and 2 cm (A, B, C, and D configurations). The other observations at 2 cm, 3.6 cm, and 6 cm were obtained to study the radio emitting starburst regions at high angular resolution.

The data were calibrated and mapped within NRAO’s Astronomical Image Processing Software (AIPS). A nearby point source, in most cases 0834-201, was observed every 10–15 minutes to calibrate the relative phases of the antennas. The radio flux density standard 3C286 (1328+207) was observed twice per observing session in order to calibrate the absolute intensities. Uncertainties on the absolute fluxes are due to the intrinsic variability of 3C286 ($\sim 1\%$; Perley 1998) and the magnitude of the closure errors on the secondary calibrator used to bootstrap the sensitivity solution from the primary flux calibrator. These errors varied with each dataset. We adopt a median of $\sim 5\%$ on the zero point of the flux calibration from epoch to epoch.

⁴The National Radio Astronomy Observatory is operated by Associated Universities, Inc., under cooperative agreement with the National Science Foundation.

3. Radio Continuum Analysis

3.1. Global Radio Spectral Properties

In order to estimate a total radio flux density at each frequency, we mapped the 92 cm, 20 cm, 6 cm, and 2 cm low resolution datasets using only antenna pairs with the shortest baselines by applying a 5 kilo- λ Gaussian UV-taper in the AIPS task IMAGR. These parameters provide the greatest sensitivity to large extended structures by weighting short UV baselines most heavily. The resulting synthesized beam has dimensions $\sim 26'' \times 24''$. The typical RMS noise in these maps is $75 \mu\text{Jy beam}^{-1}$ but much larger ($280 \text{ mJy beam}^{-1}$) at 90 cm due to lower overall sensitivity and confusion from other background sources in the $130''$ FWHM primary beam. Extensive mapping and deconvolution (CLEANing) was necessary to remove the sidelobe structure from other stronger sources within the primary beam at 90 cm. Table 2 summarizes the total radio continuum flux density of Henize 2-10 at each wavelength, as measured from the low resolution maps.

For comparison with the new results, Table 2 lists the single-dish radio continuum measurements tabulated in Allen *et al.* (1976) over a similar range in frequency. We also include the Owens Valley millimeter-wave continuum measurements at 96 GHz and 230 GHz from Meier & Turner (1999). Figure 1 displays these results graphically in a plot of integrated flux density versus frequency. In all cases, the VLA flux density is less than, but within the errors of, the single dish result at the same (interpolated) wavelength. This systematic offset is expected since aperture synthesis telescopes like the VLA lack the short UV spacings required for a total flux measurement. Since aperture synthesis arrays act as spatial filters, the data are insensitive to smooth structures larger than an angular scale set by the separation of the shortest antenna pairs. For the low-resolution configurations and wavelength combinations used here, structures larger than about $90''$ will be invisible to the VLA. The ratio of flux detected with the interferometer to single dish results (60% - 70%) is comparable to the ratios for other local starbursts observed with both types of telescopes (e.g., NGC 5253–Turner, Ho & Beck 1998). The largest discrepancy for He 2-10 occurs at 90 cm. We interpret this difference as the result of additional contributions by confusing sources in the large beam and sidelobes of the single-dish telescopes at low frequencies. The total VLA flux at 6 cm and 3.6 cm, 42.6 mJy and 24.3 mJy, respectively, may also be compared to the measurements of Méndez *et al.* (1999) using the Australia Telescope Compact Array (ATCA) at comparable wavelengths. Méndez *et al.* measure 30.3 mJy and 21.4 mJy respectively, 71% and 88% of the VLA flux. This difference may be explained as the inclusion of shorter projected UV spacings in the 6 cm C-configuration VLA dataset where baselines as short as 1 kilo-lambda are present compared to the ATCA dataset of Méndez *et al.*

In Figure 1 we show a best fit power law of the form $S_\nu \propto \nu^\alpha$, where $\alpha = -0.54$ for the VLA data, including the 96 GHz point from Meier & Turner (1999). This value is typical of star-forming galaxies like M 82 (Klein, Wielebinski, & Morsi 1988), NGC 3448 (Noreau & Kronberg 1987), and H II galaxies (Deeg *et al.* 1993) which are generally dominated by nonthermal (synchrotron) emission with $-0.8 < \alpha < -0.4$. The 3.6 cm point lies below a best fit power law to the other data, presumably because the array configuration combination is not perfectly scaled to match the UV coverage of the other datasets. The 3.6 cm dataset lacks the shortest UV spacings present in the other observations, and thus we do not consider this dataset in the further analysis of the integrated radio spectrum.

The overall radio spectral index is highly nonthermal, consistent with synchrotron radiation produced in supernova explosions. Our best-fit value of $\alpha = -0.54 \pm 0.04$ is slightly flatter than the value $\alpha = -0.60 \pm 0.15$ found by Allen *et al.* (1976) from single dish data over the range 0.4 to 10.6 GHz, and $\alpha = -0.59 \pm 0.05$ by Méndez *et al.* (1999) from two high frequency points (4.8 GHz and 8.6 GHz). Removing the 90 cm (0.325 GHz) point from the fit yields $\alpha = -0.58 \pm 0.05$, more consistent with the other estimates. The overall spectrum suggests a combination of thermal and nonthermal processes, with thermal processes dominating at frequencies of 90 GHz and above.

He 2-10 shows a low-frequency turnover in its radio spectrum similar to several of the Blue Compact Galaxies observed by Deeg *et al.* (1993). Deeg *et al.* considered several physical mechanisms to explain this low-frequency turnover. Free-free absorption of the predominantly synchrotron spectrum by thermal electrons in the halo of He 2-10 could explain this result by modifying the predominantly nonthermal spectrum at long wavelengths.

3.2. High Resolution Radio Morphology and Spectra

3.2.1. Overall Morphology

In order to investigate the radio morphology of Henize 2-10 on small angular scales, we selected the 3.6 cm (8.4 GHz) data from 1996 May 14 which provides the best combination of angular resolution, sensitivity, and UV coverage. These data have roughly 2–3 times the angular resolution of the ATCA dataset presented in Méndez *et al.* (1999) but is less suitable for measuring total fluxes or extended structures due to a relative lack of short UV spacings. Figure 2 displays a 3.6 cm (8.4 GHz) contour map made with a UVTAPER of 500 kilo-wavelengths. The RMS noise level is 35 mJy beam^{-1} . The synthesized beamsize of $0.57'' \times 0.70''$ corresponds to a linear size of $25 \times 30 \text{ pc}$ for the assumed distance of 9 Mpc.

Contours are -5, -4, -3, 3, 4, 5, 6, 8, 10, 12, 14, 16, 18, 20, and 22 times the RMS noise level. Figure 2 also shows a Hubble Space Telescope WFPC2 image obtained through the F555W filter (Johnson *et al.* 1999) presented as a logarithmic greyscale. The absolute coordinates of the radio map are accurate to $0.05''$ while the HST image are uncertain by $\sim 0.5''$, limited by the positional uncertainties of the guide stars from the Guide Star Catalog (Lasker *et al.* 1990). This leads to a relative positional uncertainty between the radio and optical images of the same amount, $0.5''$.

Figure 2 shows several radio “knots” aligned in an east-west orientation. The overall radio morphology is reminiscent of that in M 82 (Golla, Allen, & Kronberg 1996) and NGC 3448 (Noreau & Kronberg 1987) observed at similar linear resolution. We identify five radio knots which we label Knots 1 through 5 from west to east. Our Knot 4 corresponds to RC1 in the radio maps of Méndez *et al.* (1999) while our Knots 1 and 2 together comprise their RC2. Figure 2 does not show the spur of radio emission extending eastward from RC1 in the Méndez *et al.* maps, even though the data presented in Figure 2 has the same frequency and higher sensitivity (RMS= $35 \mu\text{Jy beam}^{-1}$) than the ATCA data (RMS= $150 \mu\text{Jy beam}^{-1}$). These maps do, however, show the spurs of radio emission extending northward from RC1 and RC2 (our Knots 4 and Knots 1&2), lending credence that these are real features somehow associated with the starburst events. The signal-to-noise is not sufficient in these regions to obtain a spectral index (see below) but their relative strength at 6 cm compared to 3.6 cm suggests a nonthermal origin. The proximity of these features to the nuclear star clusters is consistent with a scenario wherein wind-driven and supernovae shells sweep up and compress the magnetic field along with high-energy electrons to produce regions of enhanced synchrotron emission.

The radio knots contribute 4.4 mJy of the 24.3 mJy total at 3.6 cm. Each knot contributes just under 1 mJy to this total. They have finite deconvolved sizes less than $0.1''$ – $0.5''$ corresponding to linear sizes of 3–20 pc. Diffuse emission in Figure 2 which comprises the majority of the radio flux is nearly aligned with the optical major axis of the galaxy at 168° (Corbin, Korista, & Vacca 1996). This high resolution map contains nearly all of the flux seen in lower resolution maps made with the same dataset, but due to the lack of short spacing in the BnA configuration, 24.3 mJy should be regarded as a lower limit to the total flux at 3.6 cm as seen with a single dish.

Although there is a relative uncertainty of $0.5''$ between the radio and optical images, we can say that there is no obvious correlation between the morphology of 6–8 optical/UV star clusters (distributed in a chevron configuration) and the radio sources. Given any possible $0.5''$ translation of the optical image, no more than 2 of the radio sources would have a corresponding optical/UV counterpart. Given the high extinction in the core of

this galaxy, it is not surprising that the optical and radio morphologies are so different. The ground-based JHK infrared images of Beck *et al.* (1997) have somewhat lower ($0.9''$) resolution and do not show prominent features which could correspond to the radio knots.

3.2.2. Radio Continuum Spectral Index

In an effort to study the spectral properties of these compact structures, we mapped the high resolution 2 cm and 6 cm datasets, taking care to use only matched UV data from array configurations A and B. The only observations with sufficient quality (high resolution and good phase stability) were the A configuration 6-cm data from 1995 and B configuration 2-cm data from 1996. Because of the snapshot nature of the observations, the UV coverage is slightly different for each dataset, but the overall beamshape is nearly identical. Mapped with a Gaussian taper of ~ 500 k λ , the UV data produced a clean beam size of $0.82'' \times 0.40''$, highly elongated in the north-south direction. The UV coverage of the 3.6 cm data does not match the other datasets, so we do not consider it for comparison here.

The 2 cm and 6 cm maps appear in contour form in Figs. 3a–3b overlaid on the HST WFPC2 F555W image of the central region of He 2-10 (Johnson *et al.* 1999). Because the data are mapped to obtain the highest possible angular resolution, only the high surface brightness radio features are visible. The total flux in the maps is 17.5 mJy at 2 cm and 14.5 mJy at 6 cm, 83% and 34% respectively, of the total flux measured with lower resolution VLA configurations and mapping procedures. Table 2 records the total flux in these maps at each frequency for each dataset. From these maps it is clear that at least 6 distinct radio components make up the central region of Henize 2-10. We performed multiple Gaussian fitting with the AIPS task IMFIT to characterize the positions and relative strengths of these sources. We list the positions and fluxes of these knots in Table 3 based on elliptical Gaussian fits to maps made with the 2 cm and 6 cm datasets as described below. Uncertainties on the peak and integrated flux densities are dominated by limitations in defining the background flux levels around each knot. We estimate the total flux uncertainties at 20% based on multiple attempts to fit each component. Only five of the sources could be successfully fit and deconvolved due to the irregular background and limited angular resolution. Each of the sources has an integrated flux near 1 mJy. Table 3 shows that the compact radio sources comprise 27% (2 cm) and 9% (6 cm) of the total radio emission in Henize 2-10 as measured with the VLA. For the assumed distance of 9 Mpc, 1 mJy corresponds to a luminosity of 9.2×10^{25} erg s $^{-1}$ Hz $^{-1}$ or 9.2×10^{18} W Hz $^{-1}$. This is similar to the luminosity of young (few yr) radio supernovae reported by Weiler

et al. (1989) in a variety of local galaxies. However, we find the same radio sources present in the datasets from 1984. Although the 6 cm radio data from 1984 and 2 cm data from 1985 are of lower quality (about half the sensitivity), the strengths of the radio components are comparable, within the errors, of the more recent data. Since radio supernovae have typical decay times of a few years (Weiler *et al.* 1986), it is unlikely that these sources still present ten years later in 1996 can be such transient events.

From Figure 3 it is clear that the compact radio sources are more luminous at shorter wavelengths, and thus have an inverted (positive α) radio spectral index. Figure 4 shows a map of the spectral index, α_2^6 (where $S_\nu \propto \nu^\alpha$), constructed from the 2 and 6 cm maps which were first blanked in regions with signal-to-noise $<4:1$. The spectral index, shown in greyscale, varies from $\alpha = -0.5$ (mostly nonthermal) to $\alpha = -0.1$ (pure optically thin thermal bremsstrahlung) to $\alpha = 1.0$ (optically thick thermal bremsstrahlung). Contours show the 2 cm radio continuum from Figure 3a. Most starburst galaxies show radio spectra dominated either by synchrotron emission ($-1.2 < \alpha < -0.4$), or thermal bremsstrahlung ($\alpha = -0.1$), or some combination (e.g., Deeg *et al.* 1993). Since radio supernovae typically have negative spectral indices after several hundred days (Weiler *et al.* 1986), the positive spectral index of these sources is additional evidence that they are not young supernovae.

Might these radio sources be supernova remnants which have much longer lifetimes than the individual supernovae themselves? The luminosities of typical SNRs in the Milky Way are several orders of magnitude less luminous, ranging from 8×10^{21} erg s $^{-1}$ Hz $^{-1}$ for 1000 yr old remnants, to 7×10^{24} erg s $^{-1}$ Hz $^{-1}$ for Cas A (330 yr). Each of the five ~ 1 mJy sources is thus a factor of 10 more luminous than Cas A. At the assumed distance of He 2-10, a fairly radio-luminous young supernova remnant like Cas A would be only a 2σ detection in the current data.

M 82 also contains multiple supernova remnants making it a good object for comparison with He 2-10. With a distance of ~ 3.63 Mpc (Freedman *et al.* 1994), it can be studied at higher spatial resolution. Radio continuum maps presented in Allen & Kronberg (1998) show 26 compact sources with linear diameters of 3.5 pc ($0.2''$) and 2 cm spectral luminosities of 2.9×10^{24} erg s $^{-1}$ Hz $^{-1}$ to 7.3×10^{25} erg s $^{-1}$ Hz $^{-1}$ (fluxes of 0.2 mJy to 5 mJy). The five radio sources in He 2-10 fall at the upper end of this luminosity range. Of the 26 sources in M 82, 22 show distinctly nonthermal spectral indices and are consistent with supernova remnants. Their radio spectra often show turnovers, but only at low frequencies ($\nu < 1$ GHz), due to free-free absorption in the surrounding ionized gas. Only one source has a thermal spectrum typical of H II regions. Three sources remain unidentified. By comparison, the five radio sources in He 2-10 have large luminosities and inverted spectral indices at frequencies as high as $\nu > 5$ GHz, suggesting that none of them are individual

SNRs. Although the nonthermal nature of the global radio spectral index in He 2-10 clearly indicates that several thousand supernovae contribute to the observed synchrotron emission, the individual events are probably too old and faint to be seen except collectively.

Compact H II regions are strong sources of free-free emission and represent most plausible origin of the compact radio knots. Figures 5a & 5b show the radio continuum contours at 2 cm and 6 cm superimposed on a continuum-free HST narrowband $H\alpha$ image. The relative alignment of the two images is accurate to $\sim 0.5''$ RMS. There is no obvious correlation between the radio and $H\alpha$ features, although if the HST image is shifted $\sim 1''$ to the east, several of the radio maxima would more closely correspond to the regions of highest emission line surface brightness. Unfortunately it is not possible to unambiguously identify the radio features with $H\alpha$ counterparts. If the radio knots are due to H II regions, then the lack of correspondence with the $H\alpha$ images suggests a large amount of extinction. Narrowband near-infrared imaging in the Bracket γ line at high spatial resolution ($0.1''$) could help confirm the H II region nature of the sources.

Flat or positive spectral indices like the ones observed in He 2-10 are common for ultra-compact H II regions in the Galaxy on sub pc scales (e.g, see the compilation of Wood & Churchwell 1989a for ultra-compact H II regions), but are very unusual on larger pc-sized scales in other galaxies. Turner, Ho, & Beck (1998) report a radio source in the nucleus of NGC 5253 which has about the same luminosity as the each of the 5 sources we find in He 2-10. It has a flat spectral index consistent with mostly thermal emission. Allen & Kronberg (1998) report a radio source, 42.21+590, with a similar luminosity ($6.9 \times 10^{25} \text{ erg s}^{-1} \text{ Hz}^{-1}$) in M 82 which they identify as an H II region on the basis of its flat ($\alpha = -0.1$) radio spectral index. All five radio sources in He 2-10 show radio spectral indices greater than $\alpha = 0.0$, suggesting that their spectral energy distributions have been modified by free-free absorption.

In Figure 6 we plot the 2 cm (14.9 GHz) and 6 cm (4.8 GHz) fluxes of each source to show the rising nature of the radio spectrum toward higher frequencies. Since the absorption coefficient for free-free absorption, κ_ν , is proportional to ν^{-2} , there is a turnover frequency ν_t , where a plasma becomes optically thick to radiowave frequencies and the spectral index changes from $\alpha = -0.1$ to positive values, approaching the blackbody limit of $\alpha = 2$ as $\tau \rightarrow \infty$. The brightness temperature is given by

$$T_B(K) = \frac{F\lambda^2}{2k\Omega}, \quad (1)$$

where k is Boltzman's constant, and Ω is the beamsize. In useful units, this becomes,

$$T_B(K) = 1541.5 \times 4 \ln 2 \frac{F(Jy)\lambda^2(cm)}{\pi a''b''} \quad (2)$$

where F is the flux of the source, λ the wavelength of observation, and a and b are the major and minor FWHM of the synthesized beam in arcseconds. In the absence of detailed knowledge about the structure of each knot, we assume that the emission fills the beam uniformly. This assumption means that an estimate of the brightness temperature is necessarily a lower limit on the actual value. We find brightness temperatures between 15 K and 28 K at 2 cm, increasing to 81 to 164 K at 6 cm as summarized in Table 3. We estimate a *lower limit* on the radio optical depth by comparing the brightness temperature, T_B , of the sources to the electron temperature of the gas, T_e , using

$$T_B = T_e(1 - e^{-\tau}) \quad (3)$$

Adopting $T_e=6000$ K based on the spectroscopy of Kobulnicky *et al.* (1999) and the brightness temperatures in Table 3, we find optical depths of $\tau \geq 0.01 - 0.02$ at 6 cm. Using Mezger & Henderson (1967), the emission measure $EM = \int n_e^2 dl$ is

$$EM(cm^{-6} pc) = 0.083 \left(\frac{T_e}{(K)}\right)^{-1.35} \left(\frac{\nu}{(GHz)}\right)^{-2.1} \tau. \quad (4)$$

These knots yield emission measures in excess of $5 \times 10^4 cm^6 pc$.

In order to explore the nature of the compact sources in more detail without needing to make assumptions about the size of the emitting region, we constructed model H II regions (spherical, uniform electron density and electron temperature) of radius, R , electron temperature, T_e , an electron density, n_e . We computed the emergent radio spectrum considering only thermal Bremsstrahlung emission and self-absorption processes. In Figure 6 we show the resulting spectral energy distributions for a range of models. The luminosities and spectral indices of these compact sources are well-fit by model H II regions with a radius of 3–8 pc (0.06''–0.17''), a mean electron temperature of 6000 K, and electron densities of 1500–5000 cm^{-3} at a distance of 9 Mpc. These sizes imply that the emitting regions fill only 4% to 40% of the VLA synthesized beam. The optical depths at 4.8 GHz range between $\tau = 0.3$ and $\tau = 2.5$ for the different models. Emission measures range between $10^7 cm^6 pc$ and $10^8 cm^6 pc$. The required densities are consistent with $500 < n_e < 11000$ measured from optical spectroscopy of the nuclear regions (Hutsemekers & Surdej 1984). The model H II regions have optical depths $\tau_{5 GHz} \approx 0.4 - 3$ and $\tau_{15 GHz} \approx 0.04 - 0.3$.

We plot the spectral energy distribution of several model bremsstrahlung sources in Figure 6 to show that this range of electron densities and radii can reproduce the observed luminosities and spectral energy distributions. Such high electron densities are required to produce the large optical depth at frequencies lower than 5 GHz. The source size is constrained by the requirement to match the total luminosity of the knots and to be consistent with the upper limits on angular sizes measured in the VLA maps. Based on the large optical depths due to free-free absorption at frequencies below 5 GHz, we predict that these radio knots will be extremely faint at longer wavelengths ($< 100 \mu Jy$ at 1.4 GHz) where the optical depth should exceed $\tau_{1.4 GHz} > 20$ for some knots.

4. Energy Budget and Ionizing Stars

4.1. He 2-10 as a Whole

The total H α flux of He 2-10 reported by Beck & Kovo (1999) is $1.35 \times 10^{-10} \text{ erg s}^{-1} \text{ cm}^{-2}$ which corresponds to a luminosity of $1.2 \times 10^{42} \text{ erg s}^{-1}$ at 9 Mpc. This is about an order of magnitude higher than Méndez *et al.* (1999) who report an H α flux of $1.82 \times 10^{-11} \text{ erg s}^{-1} \text{ cm}^{-2}$. Published H α slit spectroscopy (Vacca & Conti 1992) and new HST H α imaging (Johnson *et al.* 1999) is more consistent with the latter value, so we adopt the Méndez *et al.* measurement which implies an H α luminosity of $1.6 \times 10^{41} \text{ erg s}^{-1}$ at 9 Mpc. For a case B ionization bounded nebulae in which all of the H-ionizing photons are re-emitted as Balmer series photons, the H α luminosity indicates a Lyman continuum photon production rate⁵ of $Q_{Lyc} = 1.1 \times 10^{53} \text{ s}^{-1}$. The thermal radio luminosity can be used to obtain a second estimate of Q_{Lyc} following Condon (1992),

$$\left(\frac{Q_{Lyc}}{s^{-1}}\right) \geq 6.3 \times 10^{52} \left(\frac{T_e}{10^4 \text{ K}}\right)^{-0.45} \left(\frac{\nu}{GHz}\right)^{0.1} \left(\frac{L_{thermal}}{10^{27} \text{ erg s}^{-1} \text{ Hz}^{-1}}\right) \quad (5)$$

Adopting the total measured 2 cm (15 GHz) flux of 21.1 mJy from Table 2 ($L_{2 \text{ cm}} = 1.9 \times 10^{27} \text{ erg s}^{-1} \text{ Hz}^{-1}$), we estimate $Q_{Lyc} = 2.0 \times 10^{53} \text{ s}^{-1}$, assuming that all of the 2 cm flux is due to free-free processes and adopting a mean electron temperature of 6000 K for He 2-10 (Kobulnicky, Kennicutt, & Pizagno 1999). Corrected by a factor of 1.9 (0.7 mag) for extinction⁶ the Méndez *et al.* measurement yields

⁵ We use, $Q_{Lyc} (s^{-1}) = \frac{1}{h\nu_{H\alpha}} \frac{\alpha_B(10,000 \text{ K})}{\alpha_{H\alpha}^{eff}(10,000 \text{ K})} L_{H\alpha} = 7.3 \times 10^{11} L_{H\alpha} (erg s^{-1})$. This should be regarded as a lower limit on Q_{Lyc} since the galaxies may be translucent to Lyman continuum photons.

⁶Although there are clearly large extinction variations within He 2-10, we estimate the global extinction in

$Q_{Ly\alpha} = 2.1 \times 10^{53} \text{ s}^{-1}$, consistent with the radio estimate of $Q_{Ly\alpha} = 2.0 \times 10^{53} \text{ s}^{-1}$. Assuming that a typical O star (type O7V) produces $Q_{Ly\alpha} = 1.0 \times 10^{49} \text{ s}^{-1}$ (Vacca 1994; Vacca, Garmany, & Shull 1996), then 20,000 such O stars are required to power the observed emission. This estimate is greater than the number of O5 stars derived by Vacca & Conti (1992) on the basis of nebular spectroscopy of region A, and is somewhat lower than the 31,000 O stars estimated by Conti & Vacca (1994) from UV imaging. However, the exact number of stars is highly dependent on the assumed age of the starburst, so the different methods are not necessarily in disagreement.

Adopting the conversion from $H\alpha$ luminosity to star formation rate (SFR) of Kennicutt (1983)

$$SFR(M_{\odot} \text{ yr}^{-1}) = 8.9 \times 10^{-42} L_{H\alpha} (\text{erg s}^{-1}), \quad (6)$$

we find a star formation rate of $1.4 M_{\odot} \text{ yr}^{-1}$. For the 11.9 Mpc distance adopted by Méndez *et al.* (1999) this would become $2.5 M_{\odot} \text{ yr}^{-1}$.

4.2. The Dense H II Regions

The energy requirements for each of the compact radio-emitting knots can be computed in a similar manner to the estimate for the entire galaxy, using Equation 5 above. Using the 2 cm luminosities in Table 3, we find that each knot must be powered by $5\text{--}10 \times 10^{51}$ Lyman continuum photons s^{-1} . Assuming that each O7V star produces $Q_{Ly\alpha} = 1.0 \times 10^{49} \text{ s}^{-1}$ (Vacca 1994; Vacca, Garmany, & Shull 1996), each knot requires between 500 and 1000 such stars as its energy source. Thus, each knot contains more O stars than are found in the entire 30-Doradus nebula in the LMC (~ 200 , Vacca *et al.* 1995; ~ 80 , Parker 1992). Using the Starburst 99 models of Leitherer *et al.* (1999) with solar metallicity, Salpeter IMF, an upper mass cutoff of $100 M_{\odot}$, and a lower mass cutoff of $1 M_{\odot}$, starburst knots producing this range of Lyman continuum photons at an age of 1 Myr would have masses of $0.8\text{--}1.6 \times 10^5 M_{\odot}$. These masses are consistent with those found for optical knots in He2-10 by Johnson *et al.* (1999).

Since the star-forming regions implied by these radio features are not seen even faintly on the HST V or I-band images, their visual extinctions must be quite large, $A_V > 5$. Such

He 2-10 from the $H\alpha/H\beta$ line ratios of Kobulnicky, Kennicutt, & Pizagno (1999) which suggest a logarithmic extinction parameter $c(H\beta) = 0.54$ corresponding to $A_V = 2.1c(H\beta) = 1.1$ mag and $A_{H\alpha} = 0.7$ mag for a Seaton (1979) reddening law.

large extinction values are consistent with the column density of molecular gas observed in this region (Kobulnicky *et al.* 1995) and the extinction estimates from the infrared silicate features ($A_V \simeq 30$, Phillips *et al.* 1984). Given that He 2-10 was already known to contain between 4600 (Vacca & Conti 1992; a lower limit due to the longslit spectroscopic nature of the observations) and 31,000 O stars (Conti & Vacca 1994) the additional ~ 4000 O stars contained in these five dense, heavily obscured H II regions represent a significant fraction of the massive stars in He 2-10. We list in Table 3 the $H\alpha$ luminosity of each knot based on the thermal radio continuum luminosities. From these numbers it is easy to predict Brackett γ or other emission line luminosities using recombination coefficients for hydrogen tabulated by Hummer & Storey (1987).

If all H II regions go through an enshrouded phase, it is possible to estimate the fraction of their lifetimes which these objects spend buried in their parent molecular clouds. This fraction is simply the number of O stars free of the surrounding material (which therefore can be detected in the optical bands) divided by the number of O stars which are still behind such high column densities that they are only detectable at longer wavelengths, such as the radio regime. In this case, if we adopt the number of O stars detected in the optical as 31,000 (Conti & Vacca 1994) in comparison the ~ 4000 we have detected in heavily obscured H II regions, O stars spend approximately 13% of their lives embedded in optically thick regions. This is remarkably consistent with the results of Wood & Churchwell (1989a) who find that massive stars in Galactic ultra-compact H II regions spend approximately 15% of their lives within their parent molecular clouds.

5. Discussion and Conclusions

Our major result is the discovery of multiple optically thick free-free sources, probably giant H II regions, which comprise a substantial fraction (27%) of the total radio luminosity at 15 GHz. The majority of these sources do not coincide with features visible in the optical HST images, leading us to conclude that they are heavily obscured by dust. The combination of high obscuration and high density inferred from the free-free optical depth is consistent with very dense H II regions such as the one seen in NGC 5253 (Turner, Ho, & Beck 1998). Electron densities as high as 10^5 have been measured in He 2-10 from the optical spectroscopy of Hutsemekers & Surdej (1984). While such dense, optically-thick, inverted-spectrum H II regions exist in abundance around *individual* stars in the Galaxy (i.e., ultra-compact H II regions; Wood & Churchwell 1989a) this phenomenon has not been previously seen on such large spatial and energetic scales. Because of their similar densities to ultracompact H II regions in the Galaxy, we might term them “ultra dense H II regions”

(UDH II). Their luminosities suggest that such dense H II regions harbor the youngest “super star clusters” which are observed to be ubiquitous in He 2-10 and other starburst systems (e.g., Conti & Vacca 1994; O’Connell, Gallagher, & Hunter 1994; O’Connell *et al.* 1995; de Marchi *et al.* 1997). These high densities are similar to the densities required on theoretical grounds in the birthplaces of globular clusters (Elmegreen 1999).

It is not surprising that a fraction (~ 4000 out of $5000-31,000$) of the massive stars in He2-10 are hidden by dust, perhaps in their parent molecular clouds. After all, massive stars seem to live a significant fraction of their lives ($\sim 15\%$; Wood & Churchwell 1989b) buried in their natal material. What *is* surprising, is that so *many* OB stars are located in these massive high-density H II regions in He 2-10 compared to other galaxies. He 2-10 contains 5 such H II regions containing ~ 4000 O7V equivalent stars, while the more luminous starbursts like M 82 contain one, at most (Allen & Kronberg 1998). What makes He 2-10 special? With electron densities of up to 5000 cm^{-3} compared to the $n_e \simeq 100\text{ cm}^{-3}$ observed in typical giant extragalactic H II regions, the five radio-bright H II regions in He 2-10 should have an overpressure, compared to the surrounding ionized gas with similar temperature of, $\sim 5000/100 \geq 50$. $P/k \sim 10^6$ for the typical ionized ISM in galaxies whereas $P/K \sim 10^7 - 10^8$ here. Such high pressure regions should expand rapidly to re-establish pressure equilibrium and become undetectable on timescales of $\text{few} \times 10^5$ years assuming an expansion rate equal to the sound speed, 10 km s^{-1} . Thus, they do not exist for longer than 10%-15% of the lifetime of a typical O stars unless confined by an additional external pressure greater than that in the typical ISM.

Perhaps the pressure of the infalling molecular material seen in millimeter-wave interferometer maps (Kobulnicky *et al.* 1995; Meier & Turner 1999) provides the confinement needed to prolong the lifetime of these giant, dense H II regions. Or, perhaps other compact star-forming galaxies, along with nuclear starburst systems, contain dense, heavily obscured H II regions like the five in He 2-10, but they have simply not been identified as such. One recent radio continuum study of NGC 2146 provides evidence that such high-density H II regions will be found in other galaxies as well (Tarchi *et al.* 1999). High resolution 2 cm and 6 cm radio observations of a whole sample of starburst systems acquired in scaled VLA A and B-array configurations will be required to know for certain. To date, such high spatial resolution data generally exists only for more luminous systems like quasars and AGN. We predict that sensitive multi-frequency imaging of normal starburst systems will show that this dense H II region phenomena is simply a normal, but short-lived phase in the chronology of a starburst. The short lifetime implied for such structures means that their presence is an unmistakable signature of the youngest (< 1 Myr) super starclusters. Since super starclusters are proposed to be young versions of globular clusters, we may be seeing the birth of globular clusters in the nucleus of Henize

2-10.

Special thanks to David E. Hogg for sharing his 1984-1985 epoch VLA observations and for helpful comments on the manuscript. We acknowledge the delightful atmosphere, stimulating conversations and inspiration from colleagues at IAU Symposium 193 on Wolf-Rayet Phenomena in Galaxies in Puerto Vallarta, November 1998, especially Sara Beck, David Méndez, Cesar Esteban, David Meier, and Jean Turner. It is also our pleasure to thank Peter Conti and Bill Vacca for continued discussions with us on these subjects. We thank Uli Klein for comments on a draft manuscript and for sharing the results of a similar radio study of NGC 2146 in advance of publication. We thank David Méndez and David Meier for sharing results and data in advance of publication. H. A. K. thanks Evan Skillman and John Dickey for guidance and encouragement advice during the early phases of this project. H. A. K. is grateful for support from a NASA Graduate Student Researchers Program fellowship and a Hubble Fellowship #HF-01094.01-97A awarded by the Space Telescope Science Institute which is operated by the Association of Universities for Research in Astronomy, Inc. for NASA under contract NAS 5-26555. K. E. J. is pleased to acknowledge support for this work provided by NASA through a Graduate Student Researchers Fellowship and grant GO-06580.0195A.

REFERENCES

- Allen, D. A., Wright, A. E., & Goss, W. M. 1976, *MNRAS*, 177, 91
- Allen, M. L., & Kronberg, P. P. 1998, *ApJ*, 502, 218
- Baas, F., Israel, F. P., & Koornneef, J. 1994, *A&A*, 284, 403
- Beck, S. C., Kelly, D. M., & Lacy, J. H. 1997, *AJ*, 114, 585
- Beck, S. C., & Kovo, O. 1999, *AJ*, 117, 190
- Caplan, J., & Deharveng, L. 1986, *A&A*, 155, 297
- Condon, J. J. 1992, *ARA&A*, 30, 575
- Conti, P. 1991, *ApJ*, 377, 115
- Conti, P. S., & Vacca, W. D. 1994, *ApJ*, 423, L97
- Corbin, M. R., Korista, K. T., & Vacca, W. D. 1993, *AJ*, 105, 1313
- Deeg, H.-J. 1993, Ph.D. Thesis, University of New Mexico
- Deeg, H.-J., Brinks, E., Duric, N., Klein, U., & Skillman, E. D. 1993, *ApJ*, 410, 626

- de Vaucouleurs, G, de Vaucouleurs, A., & Corwin, H. G., Buta, R., Paturel, G., & Fouque, P. 1991, Third Reference Catalog of Bright Galaxies, Springer, New York
- De Marchi, G., Clampin, M., Greggio, L., Leitherer, C., Nota, A., & Tosi, M. 1997, ApJ, 479, 27
- Elmegreen, B. 1999, private communication
- Freedman, W., *et al.* 1994, ApJ, 427, 628
- Golla, G., Allen, M. L., & Kronberg, P. P. 1996, ApJ, 473, 244
- Guzman, R., Jangren, A., Koo, D. C., Bershad, M. A., & Simard, L. 1998, ApJ, 495, L13
- Guzman, R., Koo, D. C., Faber, S. M., Illingworth, G. D., Takamiya, M., Kron, R. G., & Bershad, M. A. 1996, ApJ, 460, L5
- Hummer, D. G., & Storey, P. J. 1987, MNRAS, 224, 801
- Hutsemekers, D., & Surdej, J. 1984, A&A, 133, 209
- Israel, F. P., & Kennicutt, R. C. 1980, ApJ, 21, 1
- Johnson, K. E., Vacca, W. D., Leitherer, C., & Conti, P. S. 1999, in prep
- Johansson, I. 1987, A&A, 182, 179
- Klein, U., Wielebinski, R., & Morsi, H. W. 1988, A&A, 190, 41
- Kobulnicky, H. A., Dickey, J. M., Sargent, A. I., Hogg, D. E., & Conti, P. S. 1995, AJ, 110, 116
- Kobulnicky, H. A., Kennicutt, R. C., & Pizagno, J. L. 1999, ApJ, 514, 544
- Koo, D. C., Guzman, R., Faber, S. M., Illingworth, G. D. Bershad, M. A., Kron, R. G., & Takamiya, M. 1995, ApJ, 440, L49
- Lasker, B. M., Surch, C. R., McLean, B. J., Russel, J. L., Jenkner, H., & Shara, M. M. 1990, AJ, 99, 2019
- Leitherer, C., Schaerer, D., Goldader, J. D., González Delgado, R. M., Robert, C., Fokun, D., de Mello, D. F., Devost, D., & Heckman, T. M. 1999, ApJS, in press
- Lequeux, J., Maucherat-Joubert, M., Deharveng, J. M., & Kunth, D. 1981, A&A, 103, 305
- Marlowe, A. T., Heckman, T. M., Wyse, R. M., & Schommer, R. 1995, ApJ, 438, 563
- Martin, C. L. 1998, ApJ, 506, 222
- Marzke, R. O., Da Costa, L. N., Pellegrini, P. S., Willmer, N. A., Geller, M. J. 1998, ApJ, 503, 617
- Meier, D., & Turner, J. L 1999, in prep

- Méndez, D. I., Esteban, C., Filipovic, M. D., Ehle, M., Haberl, F., Pietsch, W., & Haynes, R. F. 1999, in press
- Mezger, P. G., & Henderson, A. P. 1967, ApJ, 147, 471
- Noreau, L., & Kronberg, P. P. 1987, AJ, 93, 1045
- O’Connell, R. W., Gallagher, J. S. III, Hunter, D. A. 1994, ApJ, 433, 650
- O’Connell, R. W., Gallagher, J. S. III, Hunter, D. A., & Colley, W. E. 1995, ApJ, 446, 10
- Parker, J. W. M. 1992, PASP, 106, 1471
- Perley, R. 1998, private communication
- Phillips, A. C., Guzman, R., Gallego, J., Koo, D. C., Lowenthal, J. D., Vogt, N. P., Faber, S. M., & Illingworth, G. D. 1997, ApJ, 489, 543
- Phillips, M. M., Aitken, D. K., & Roche, P. F. 1984, MNRAS, 207, 25
- Seaton, M. J. 1979, MNRAS, 187, 73p
- Tarchi, A. *et al.* 1999, in prep
- Turner, J. L., Ho, P. T. P., & Beck, S. C. 1998, AJ, 116, 1212
- Vacca, W. D., & Conti, P. S. 1992, ApJ, 401, 533
- Vacca, W. D. 1994, ApJ, 421, 140
- Vacca, W. D., Garmany, C. D., & Shull, J. M. 1996, ApJ, 460, 914
- Vacca, W. D., Robert, C., Leitherer, C., & Conti, P. 1995, ApJ, 444, 647
- Weiler, K. W., Sramek, R. A., Panagia, N., van der Hulst, J. M., & Salvati, M. 1986, ApJ, 301, 790
- Weiler, K. W., Panagia, N., Sramek, R. A., van der Hulst, J. M., Roberts, M. S., & Nguyen, L. 1989, ApJ, 336, 421
- Wood, D. O., & Churchwell, E. 1989b, ApJ, 340, 265
- Wood, D. O., & Churchwell, E. 1989a, ApJS, 69, 831

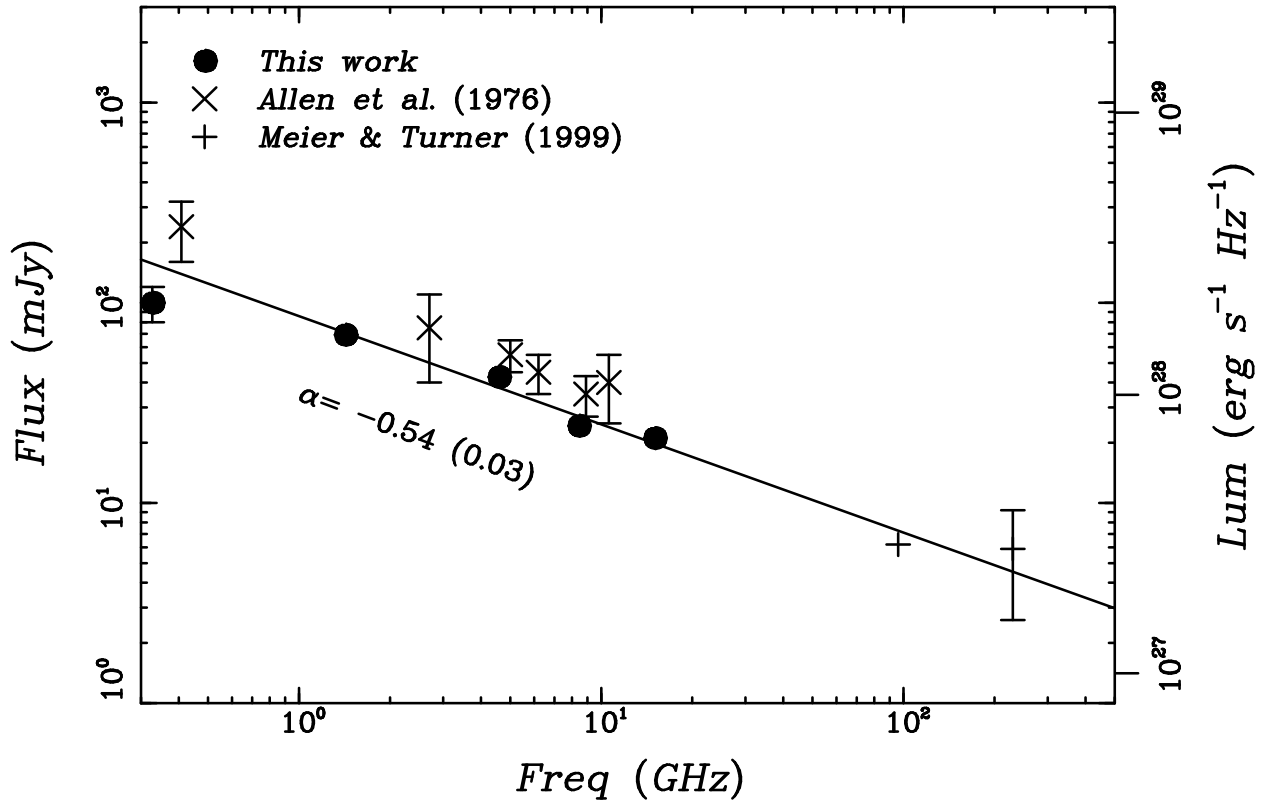


Fig. 1.— Global radio continuum fluxes of Henize 2-10 as a function of frequency. Filled circles denote data from the VLA measurements reported here, and x’s denote the single-dish measurements from Allen *et al.* (1976). The best fit power law to the VLA data, including the 96 GHz point from Meier & Turner 1999 ($S_\nu \propto \nu^\alpha$) has a slope of $\alpha = -0.54 \pm 0.03$. This slope indicates that nonthermal processes are the dominant source of radio luminosity, as is typical of starforming systems (e.g., Deeg *et al.* 1993).

Fig. 2.— Hubble Space Telescope WFPC2 F555W broadband image of Henize 2-10 (greyscale; Johnson *et al.* 1999) and a VLA 3.6 cm radio continuum map (contours) with a synthesized beamsize of $0.70'' \times 0.57''$ FWHM. Contours levels are -5, -4, -3, 3, 4, 5, 6, 8, 10, 12, 14, 16, 18, 20, and 22 times the RMS noise level of $35 \mu\text{Jy beam}^{-1}$. The beamshape appears at lower left. The greyscale representation is logarithmic, in arbitrary units. The absolute coordinates of the radio and HST images are good to $\leq 0.1''$ and $\sim 0.5''$ respectively, so that the relative positions are uncertain by $0.5''$ RMS. Five distinct radio sources are visible. The lack of a strong correlation between the radio and optical morphology suggests dust extinction is a significant factor.

Fig 3a— Hubble Space Telescope WFPC2 F555W broadband image of Henize 2-10 (greyscale) and a VLA B configuration 2 cm radio continuum map (contours) with a synthesized beamsize of $0.82'' \times 0.40''$ FWHM shown at lower left. Contours levels are -5, -4, -3, 3, 4, 5, 6, 8, 10, 12, 14, 16, 18, 20, and 22 times the approximate RMS noise level of $50 \mu\text{Jy beam}^{-1}$. Fig 3b— HST WFPC2 F555W broadband image of Henize 2-10 (greyscale) and a VLA A configuration 6 cm radio continuum map (contours) with a synthesized beamsize of $0.82'' \times 0.40''$ FWHM shown at lower left. Contours levels are -5, -4, -3, 3, 4, 5, 6, 8, 10, 12, 14, 16, 18, 20, and 22 times the approximate RMS noise level of $50 \mu\text{Jy beam}^{-1}$. The five prominent radio sources are stronger at 2 cm than 6 cm, characteristic of optically-thick thermal Bremsstrahlung sources. endfigure

Fig 4—Spectral index map (greyscale) made from the 2 cm and 6 cm high resolution maps superimposed on the 2 cm contour map from Figure 3a. Only the highest surface-brightness regions appear in these maps. The input 2 cm and 6 cm maps were each clipped at 4σ so that the regions with spectral index uncertainties, $\Delta\alpha_2^6$, larger than 0.17 are blanked. The spectral indices, α_2^6 range from $\alpha = -0.5$ (mostly nonthermal) to $\alpha = -0.1$ (pure optically thin thermal bremsstrahlung) to $\alpha = 1.0$ (optically thick thermal bremsstrahlung). The spectral and luminosity characteristics of these sources are most consistent with dense ($n_e > 1500 \text{ cm}^{-3}$) H II regions.

Fig 5a— $H\alpha$ narrowband image of Johnson *et al.* (1999) with the 2 cm radio continuum from Figure 3a in contours. The $H\alpha$ image is shown as a logarithmic greyscale in arbitrary units. There is no clear correspondence between radio features and $H\alpha$ features, but the relative alignment of the two images is accurate to only $0.5''$ RMS. Shifting the $H\alpha$ image to the east by $\sim 1''$ would produce a reasonably good correspondence between the radio and emission line maxima, but the different morphologies suggest large amounts of extinction in the nucleus. Infrared emission line imaging could confirm the presence of highly obscured, young ($< 500,000 \text{ yr}$) H II regions which are seen here only in the radio continuum. Fig 5b— $H\alpha$ narrowband images of Johnson *et al.* (1999) with the 6 cm radio continuum from Figure 3b in contours.

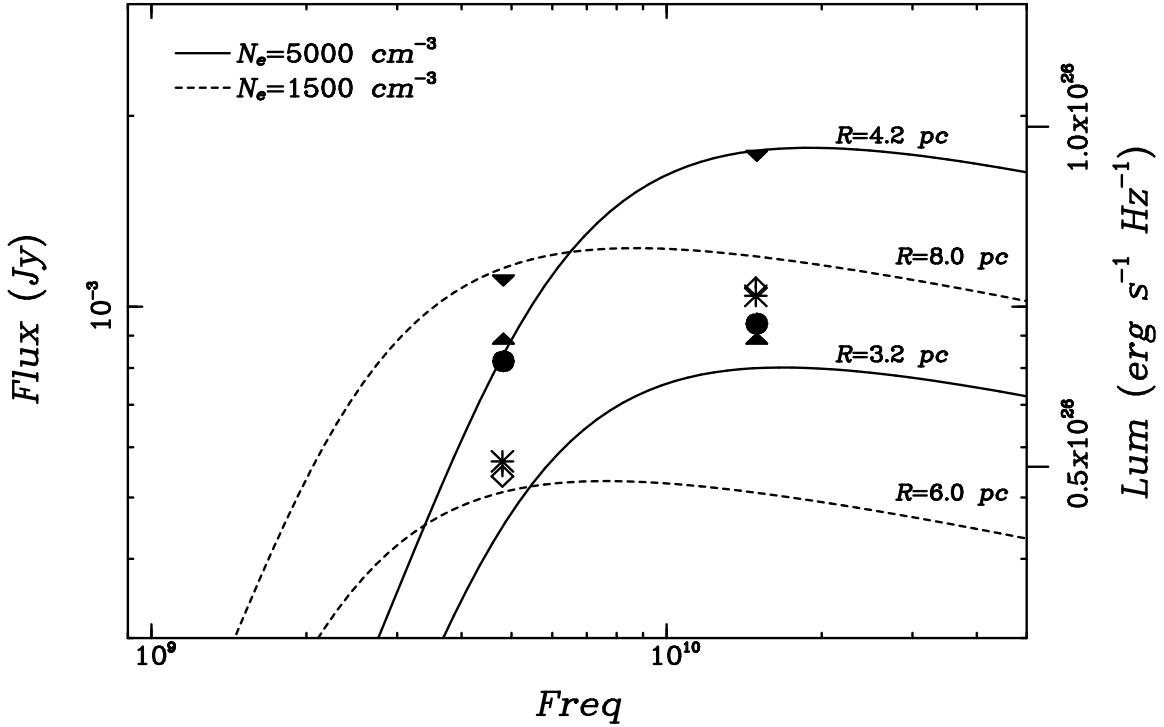


Fig 6—VLA 6cm (4.8 GHz) and 2 cm (14.9 GHz) fluxes and luminosities for the five radio knots in Henize 2-10. A different symbol represents data for each knot listed in Table 3. Solid and dotted lines represent thermal bremsstrahlung plasmas modeled as spheres of radius, R , electron temperature $T_e=6000$ K, and mean electron densities of 1500 cm^{-3} and 5000 cm^{-3} respectively. Such high densities are required to produce a sufficiently large free-free opacity needed to explain the rising spectral index between 4.8 GHz and 14.9 GHz. Thermal bremsstrahlung sources (i.e., H II regions) with radii between 3 pc and 8 pc are consistent with the imaging data and can reproduce the range of spectral shapes and luminosities of the radio knots. These high densities imply an overpressure compared to typical warm ionized medium pressures. Such H II regions should expand and become undetectable in the thermal radio continuum on timescales of 500,000 yr.

TABLE 1
VLA OBSERVATIONAL PARAMETERS

Date	Config.	freq. (GHz)	BW (MHz)	λ (cm)	Int. Time (min)	Comments
Low Resolution Configurations						
1993 Dec 20	D	15.0	2x50	2	15	ok
1994 Oct 23	C	4.58	2x50	6	15	ok
1994 May 14	BnA	1.420	20x0.024	21	240	ok
1994 Apr 25	A	0.327	2x50	92	24	ok
High Resolution Configurations						
1984 Dec 05	A	15.0	1x25	2	110	low S/N; not used
1996 Jan 02	B	15.0	2x50	2	145	ok
1996 Jan 02	B	8.41	2x50	3.6	36	low S/N; not used
1994 May 14	BnA	8.41	2x50	3.6	36	ok
1995 Jun 30	A	4.58	2x50	6	71	ok
1984 Dec 05	A	4.58	1x25	6	60	low S/N; not used

TABLE 2
HENIZE 2-10 INTEGRATED RADIO FLUX

Frequency (GHz)	Flux ^a (mJy)	Flux ^b (mJy)	Lum ^c ($\times 10^{27} \text{erg s}^{-1} \text{Hz}^{-1}$)	Flux ^d (mJy)	Flux ^e (mJy)
230	5.9±3.3 ^f				
96.0	6.2±0.6 ^f				
14.9	21.1±1.2	...	1.9±0.19	17.5±0.7	5.7
10.6	...	40±15	
8.9	...	35±8	
8.4	24.3±2.4	...	2.2±0.2	15.6±0.4	4.4
6.2	...	45±10	
5.0	...	55±10	
4.8	42.6±4.3	...	3.9±0.4	14.5±0.3	3.9
2.7	...	75±35	
1.4	69.2±6.9	...	6.3±0.6	...	
0.408	...	240±80	
0.325	100±20	...	9.2±1.8	...	

^aData from this paper, using low resolution VLA configurations and mapping parameters which yield a synthesized beam of $\sim 25''$ FWHM.

^bFrom the single-dish Allen *et al.* 1976 compilation of single-dish measurements for comparison

^cMonochromatic radio luminosity based on a distance of 9 Mpc. 1 Jy = $9.16 \times 10^{21} \text{W Hz}^{-1}$ or $9.16 \times 10^{28} \text{erg s}^{-1} \text{Hz}^{-1}$ at that distance.

^dTotal flux measured in the high resolution maps shown in Figure 2 and Figures 3a–b which are made from a restricted subset of the visibility data to ensure matched UV coverage.

^eContribution from the 5 compact radio knots only, as measured by Gaussian deconvolution and recorded in Table 3. Uncertainties are $\sim 20\%$, and are dominated by the variable background levels surrounding the knots.

^fFrom the Owens Valley Radio Observatory millimeterwave interferometer measurements of Meier & Turner (1999)

TABLE 3
PROPERTIES OF INDIVIDUAL RADIO KNOTS

	Knot 1	Knot 2	Knot 3	Knot 4	Knot 5
RA (2000) ^a	08 36 15.014	08 36 15.060	08 36 15.127	08 36 15.234	08 36 15.308
DEC(2000) ^a	-26 24 33.81	-26 24 33.98	-26 24 34.13	-26 24 34.00	-26 24 34.61
Peak _{2 cm} (mJy/bm) ^b	0.70±0.14	0.53±0.10	0.56±0.11	1.03±0.20	0.69±0.14
Peak _{6 cm} (mJy/bm) ^b	0.82±0.16	0.48±0.10	0.53±0.11	0.62±0.12	0.39±0.08
S _{2 cm} (mJy) ^b	0.94±0.19	1.06±0.21	0.89±0.18	1.73±0.34	1.04±0.21
S _{6 cm} (mJy) ^b	0.82±0.16	0.56±0.11	0.89±0.18	1.10±0.22	0.57±0.12
α ₂ ⁶	0.11±0.14	0.53±0.14	0.00±0.14	0.38±0.14	0.51±0.14
L _{2 cm} (x10 ²⁵ erg s ⁻¹ Hz ⁻¹) ^c	8.6±1.7	9.7±2.0	5.2±1.0	9.5±1.9	6.3±1.2
L _{6 cm} (x10 ²⁵ erg s ⁻¹ Hz ⁻¹) ^c	7.5±1.5	5.1±1.0	8.1±1.6	10.1±2.0	5.2±1.0
T _b (2 cm) ^d	>16	>18	>15	>29	>18
T _b (6 cm) ^d	>122	>84	>135	>164	>85
Q _{Lyα} (10 ⁵¹ photons s ⁻¹) ^e	8.9	10.0	5.4	9.9	6.5
N _* (O7V) ^f	890	1000	540	990	650
L(H α) x10 ⁴⁰ erg s ⁻¹ ^g	1.2	1.4	0.7	1.4	0.9

^aAs measured from a Gaussian fit to the 2 cm map shown in Figure 3a.

^bAs measured from a 2-D Gaussian fit to the maps shown in Figure 3a-b. Approximate 1 σ uncertainties are 20%.

^cFor an assumed distance of 9 Mpc.

^dFor the brightness temperature, we use the beamsize and peak flux of the maps in Figure 3. $T_B(K) = \frac{F\lambda^2}{2k\Omega}$ where k is Boltzman's constant, and Ω is the beamsize. In useful units, this becomes $T_B(K) = 1541.5 \times 4 \ln 2 \frac{F(Jy)\lambda^2(cm)}{\pi a'' b''}$ where F is the flux of the source, λ the wavelength of observation, and a and b are the major and minor FWHM of the source. In the absence of information about the actual source structure or size, we can only set an upper limit on the actual source by assuming that it uniformly fills the synthesized beam, 0.8'' \times 0.40''. This leads to a lower limit on the brightness temperature.

^eThe number of Lyman continuum photons implied by the 2-cm (15 GHz) luminosity via Equation 2, assuming that the 2-cm luminosity for each knot is entirely thermal in origin.

^fThe number of O7V stars required to produce the derived number of Lyman continuum photons, assuming each star emits 1.0 \times 10⁴⁹ s⁻¹ (Vacca 1994).

^gThe predicted H α luminosity of each knot based on the number of Lyman continuum photons derived above.